










# Structure, hardness, and corrosion behavior of Al- $x$ Mo ( $x = 0, 10, 30$ wt.%) binary alloys prepared by high-frequency magnetic melting

Amel Gharbi<sup>1,2</sup> , Oualid Ghelloudj<sup>3\*</sup> , Amar Ayad<sup>4</sup> , Khedidja Bouhamla<sup>1</sup> ,  
Mohamed Yacine Debili<sup>5</sup> , Jiaojiao Yi<sup>6</sup> , Houceme Bendriss<sup>2</sup>, Chems Eddine Ramoul<sup>1</sup> ,  
Sihem Ouchenane<sup>7</sup> , Saleh Remili<sup>1</sup> 

<sup>1</sup>Research Center in Industrial Technology CRTI, P.O.Box 64, Cheraga 16014 Algiers, Algeria

<sup>2</sup>Foundry Laboratory, Badji Mokhtar – Annaba University, P.O.Box 12, 23000 Annaba, Algeria

<sup>3</sup>Research Laboratory of Advanced Technology in Mechanical Production LRTAPM, Badji Mokhtar – Annaba University, P.O.Box 12, 23000 Annaba, Algeria

<sup>4</sup>Energy Systems Technology Laboratory LTSE, Higher National School of Technology and Engineering, Annaba 23000, Algeria

<sup>5</sup>Laboratory of Magnetism and Spectroscopy of Solids LM2S, Department of Physics, Badji Mokhtar – Annaba University, P.O.Box 12, 23000 Annaba, Algeria

<sup>6</sup>Laboratory of Advanced Multicomponent Materials, School of Mechanical Engineering, Jiangsu University of Technology, Changzhou, 213001, P. R. China

<sup>7</sup>Departement of chemistry, Laboratory of Inorganic Materials Chemistry, Badji Mokhtar – Annaba University, P.O.Box 12, 23000 Annaba, Algeria

Received 16 February 2025, received in revised form 13 October 2025, accepted 28 October 2025

## Abstract

This study investigated the influence of Mo addition on the structure, hardness, and corrosion behavior of Al- $x$ Mo alloy ( $x = 0, 10, 30$  wt.%) produced by high-frequency magnetic melting. Variations in microstructure, hardness, and corrosion behavior in a 3.5 % NaCl solution were studied. The results show that the high-frequency induction melting technique increases the solubility of Mo in Al from 0.07 to 0.35 at.% Mo. The 10 wt.% Mo addition induces the formation of Al<sub>12</sub>Mo and Al<sub>5</sub>Mo( $r$ ) intermetallic phases, while the 30 wt.% Mo addition leads to the appearance of a new, molybdenum-rich Al<sub>17</sub>Mo<sub>5</sub> intermetallic phase. The increase in Mo content shifts the corrosion potential towards nobler values and decreases the corrosion current density from 0.85  $\mu\text{A cm}^{-2}$  for Al to 0.29  $\mu\text{A cm}^{-2}$  for the Al-30 wt.% Mo alloy. Additionally, an improvement in polarization resistance was observed, reaching 2812  $\Omega$  for the Al-30 wt.% Mo alloy.

**Key words:** high-frequency magnetic melting, Al-Mo, intermetallic, corrosion, microstructure

## 1. Introduction

Selecting appropriate materials in modern industries generally depends on a series of criteria, including their mechanical and physicochemical properties, ease of processing, economics, and environmental compatibility. Among the various considerations, lightweight properties have drawn significant attention to Al and Al alloys in the aerospace, space, auto-

motive, agricultural, and domestic sectors [1–3]. However, the service temperature of conventional Al alloys can hardly exceed 180 °C, which is commonly attributed to the deterioration in strengthening induced by temperature-induced changes in the secondary phase. Specifically, the mechanical strength of these conventional alloys is achieved by blocking the movement of dislocations through the presence of second-phase particles dispersed in the matrix. Natu-

\*Corresponding author: e-mail addresses: [oualid.ghelloudj@univ-annaba.dz](mailto:oualid.ghelloudj@univ-annaba.dz) or [ghelloudj23@gmail.com](mailto:ghelloudj23@gmail.com)

rally, the size, morphology, distribution, and volume fraction of the second-phase particles, together with the feature of the interfaces between the matrix and the dispersed particles, determined the strengthening effect of the particle-containing alloys [4]. Furthermore, additional strengthening can be achieved through the presence of a solid solution in the matrix and grain size refinement. Apparently, in all these alloys, variations in germination and growth times during the precipitation process would dramatically affect the mechanical properties of the Al alloys. Thus, for high-temperature applications, dispersoids with excellent thermal stability are necessary to introduce into Al alloys to stabilize mechanical properties in elevated-temperature industrial environments [5, 6].

From a metallurgical perspective, the incorporation of elements with low solubility and low diffusivity should reduce precipitate coalescence kinetics in Al alloys, thereby making it more difficult to modify the driving force, i.e., the interfacial energy between the precipitates and the matrix. Accordingly, the traditional additive elements can be artificially bifurcated into two classes: the elements with relatively active chemical properties, such as copper (Cu), magnesium (Mg), zinc (Zn) and manganese (Mn), which commonly possess relatively high solubility and high diffusion ability, whereas the transition elements, such as iron (Fe), molybdenum (Mo), vanadium (V), niobium (Nb), chromium (Cr), titanium (Ti), nickel (Ni) and rare earths such as cerium (Ce), are preferred due to its low diffusivity in Al and relatively limited solid solubility [7]. Thus, through introducing the transition metals (M), the Al-rich  $Al_xM_y$  type binary phases with relatively high stability should be preferentially formed in the Al-matrix, due to which the high-temperature strength and wear resistance of Al alloys can be efficiently enhanced, endowing them with excellent durability, even over the long term [6, 8]. By contrast, Mo belongs to an important transition element that, due to its low diffusivity and limited solubility in Al, promotes the formation of dispersoids that effectively block dislocations within dendritic grains, thereby greatly improving the mechanical properties of Al alloys. Consequently, although the potential effect of Mo on Al is significant, research into Al-Mo alloys remains relatively limited [8, 9]. Specifically, the investigations associated with the Al-Mo system mainly consist of two solid solution phases,  $\alpha$ Al,  $\alpha$ Mo, a liquid phase, and the intermetallic phases  $Al_xMo_y$  ( $Al_{12}Mo$ ,  $Al_6Mo$ ,  $Al_5Mo$ ,  $Al_{17}Mo_4$ ,  $Al_{22}Mo_5$ ,  $Al_4Mo$ ,  $Al_{63}Mo_{37}$ , and  $AlMo_3$ ) [11–15]. It was found that the specific stoichiometric ratio of the Al-Mo alloy is crucial for precipitate formation.

Besides modifying the composition of Al-based alloys, the preparation techniques also determined the high-temperature applications of Al-Mo alloys. In retrospect, the alloys have been developed using several

techniques. Zdujic et al. [16] produced Al- $x$ Mo alloys ( $x = 3, 10, 17, 20, 27, 50$ , and 75 at.% Mo) by powder metallurgy. Grinding produced a fine structure with a nanometer-sized grain, forming a supersaturated solid solution of Mo in Al at concentrations of 3, 10, 17, 20, 27, and 50 at.% Mo, and a solution of Al in Mo for the concentration of 75 at.% Mo. Lee et al. [17] studied the formation of Al-Mo intermetallic particle-hardened Al alloys from a mixture of Al and Mo powders using Friction Stir Processing (FSP). It was found that FSP favored the exothermic reaction between Al and Mo, producing mainly  $Al_{12}Mo$  particles with a small quantity of  $Al_5Mo$ , due to substantial shear deformation. Abu-Zeid et al. [18] investigated spray-coated Al-Mo coatings. The addition of Mo improved tribological properties and corrosion resistance, with friction coefficients as low as 0.18 for Mo contents above 80 %. Increasing Mo content also reduces the tendency to corrosion, shifting the corrosion potential towards more noble values. Logan et al. [19] reported that, in rapidly cooled Al-Mo alloys, single-phase alloys can be obtained with up to 1.3 at.% Mo, while metastable phases appear above this concentration. These have been identified as a cubic diamond phase and a hexagonal phase, with a maximum supersaturation of 2.45 at.% Mo. On annealing, the solid solutions and intermediate metastable phases transform directly into a solid solution rich in Al and  $Al_{12}Mo$ . Chang et al. [20] studied solid solutions of Mo in Al containing 0.7 and 2.2 at.% Mo, prepared by melt spinning and annealed between 350 and 650 °C. They found that annealing induces the formation of  $Al_{12}Mo$  precipitates at grain boundaries, either through the generation of dislocation lattices in 2.2 at.% Mo alloys, or through grain boundary migration in 0.7 at.% Mo alloys. Almeida et al. [21] studied Al-Mo alloys, produced by laser surface alloying with compositions ranging from 14.8 to 19.1 wt.% Mo. They reported that the microstructure of these alloys consists of  $Al_5Mo(r)$  intermetallic particles dispersed in an Al matrix, and that hardness and wear resistance increase with the volume fraction of intermetallic compounds.

Thus, in the present work, a series of Al-Mo alloys with different Mo concentrations (10 and 30 wt.% Mo) was prepared using a high-frequency magnetic melting method. This technique permits rapid melting of these alloys while improving the interaction between Al and Mo, despite the significant difference between their melting points.

## 2. Experimental methods

Powder mixtures of Al-10 wt.% Mo and Al-30 wt.% Mo, denoted as Al-10Mo and Al-30Mo, respectively, were prepared from a mixture of high-purity metal

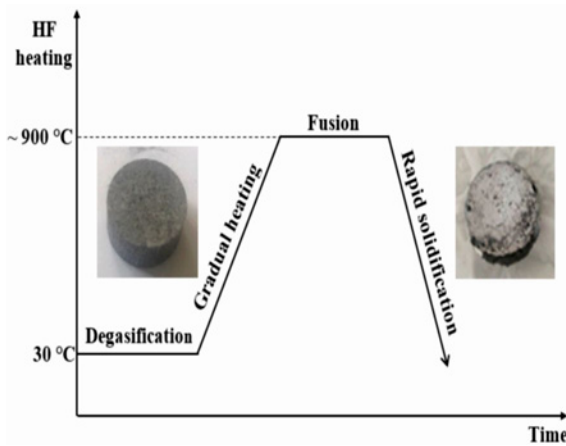


Fig. 1. Melting cycle of studied alloys in the induction furnace (HF).

powders Al (> 99 wt.%) and Mo (> 99 wt.%). The total mass of each sample is 3 g. The powders were weighed using a KERN ALS220-4N analytical balance, with a precision of  $\pm 0.1$  mg. A SPECAC-GS2511 hydraulic press was used to compact the homogeneous mixture of Al and Mo powders from each sample under a force of 10 tons. The sample obtained after compaction is a dense pellet measuring 13 mm in diameter and 5 mm in height.

The pellet is placed in a cylindrical alumina crucible, which is then inserted into a quartz tube placed inside the inductor of a Lin Therme 600 high-frequency electromagnetic induction (HF) furnace. At a frequency of 300 kHz and a power of 6 kW, the samples are melted in a vacuum generated by an EDWARDS pump. The alloy melting cycle in the high-frequency induction furnace is shown in Fig. 1.

For metallographic examination, the samples were mechanically polished using abrasive papers of different grit sizes (320 to 2400), followed by finish polishing with 3  $\mu\text{m}$  diamond paste. Etching was carried out using Killer solution (2.5 %  $\text{HNO}_3$ , 1.5 %  $\text{HCl}$ , 1 %  $\text{HF}$ , and 95 %  $\text{H}_2\text{O}$ ). For metallographic analysis, we used a Nikon ECLIPSE LV100ND optical microscope and a Quanta scanning electron microscope (SEM) equipped with an energy dispersive microanalyzer (EDS).

XRD diffractograms ( $I$ ,  $2\theta$ ) were obtained using a Philips-type diffractometer with a  $2\theta$  scan from  $20^\circ$  to  $100^\circ$  and a step size of  $0.02^\circ$ , using a copper anticathode ( $\lambda K\alpha = 1.54 \text{ \AA}$ ).

Electrochemical measurements were performed using an Autolab PGSTAT302N potentiostat/galvanostat, controlled by a computer and *Nova 2.0 software*. The electrochemical study of Al-Mo alloys was carried out in a three-electrode cell: a saturated calomel (KCl) reference electrode, a platinum counter electrode, and a working electrode. The alloys were mechanically polished using abrasive papers of decreas-

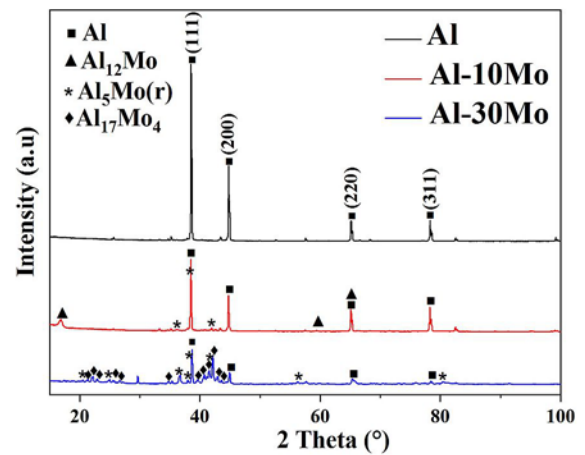


Fig. 2. X-ray diffraction spectra of Al- $x$ Mo ( $x = 0, 10, 30$  wt.%) alloys.

ing particle size (from 1000 to 4000). The prepared samples were cleaned with ethanol, then rinsed with distilled water. Tests were carried out at room temperature in a 3.5 % NaCl solution. Potentiodynamic curves were recorded by varying the electrode potential from  $-1200$  to  $+800$  mV at a scan rate of  $1 \text{ mV s}^{-1}$ . Electrochemical impedance spectroscopy (EIS) measurements were performed over a frequency range from 100 kHz to 10 mHz with a signal amplitude of 10 mV.

### 3. Results and discussion

#### 3.1. X-ray diffraction analysis

To analyze the phase component, the X-ray diffractograms of pure Al and binary alloys Al-10 wt.% Mo and Al-30 wt.% Mo, produced by high-frequency magnetic melting, were meticulously carried out, as shown in Fig. 2. Note that the pure Al diffractogram reveals diffraction peaks corresponding to the Al crystallographic ( $hkl$ ) planes, indicating good crystallinity. The most intense diffraction peak is that of the (111) Al plane, observed at an angular position  $2\theta = 38.61^\circ$ . By contrast, the addition of Mo apparently reduces the intensity of Al peaks, and the emerged diffractograms highlight the presence of diffraction peaks corresponding to the  $\alpha$ -Al solid solution, which conserves the same face-centered cubic (FCC) structure as pure Al. Furthermore, diffraction peaks associated with  $\text{Al}_x\text{Mo}_y$  intermetallic compounds, including  $\text{Al}_{12}\text{Mo}$ ,  $\text{Al}_5\text{Mo}$ , and  $\text{Al}_{17}\text{Mo}_4$ , are observed, which is consistent with the phase equilibrium diagram of the Al-Mo system [21].

With 10 wt.% Mo addition, the intermetallic phases, corresponding to  $\text{Al}_{12}\text{Mo}$  and  $\text{Al}_5\text{Mo}(r)$ , can be unambiguously observed in the XRD patterns. The  $\text{Al}_{12}\text{Mo}$  phase is a stable compound at room

temperature up to a content of around 7.6 at.% Mo (22.6 wt.%). This phase, the richest in Al, has a centered cubic structure with a lattice parameter of 7.573–7.581 Å, corresponding to the  $Im\bar{3}$  space group. Its density is around  $3.20 \text{ g cm}^{-3}$ , corresponding to a unit cell containing 26 atoms. Moreover, the  $\text{Al}_{12}\text{Mo}$  phase remains stable at temperatures below  $700^\circ\text{C}$  [22]. The  $\text{Al}_5\text{Mo}(r)$  phase is one of three allotropic forms of the  $\text{Al}_5\text{Mo}$  phase, specific to low temperatures. The other two forms are  $\text{Al}_5\text{Mo}(h)$ , stable at high temperatures, and  $\text{Al}_5\text{Mo}(h')$ , stable at intermediate temperatures. The  $\text{Al}_5\text{Mo}(r)$  phase, identified by X-ray diffraction, is a stacking variant of the  $\text{Al}_5\text{Mo}(h)$  phase. It is characterized by crystal parameters  $a = 0.4951 \text{ nm}$  and  $c = 2.623 \text{ nm}$ , a  $R\bar{3}c$  space group, and a  $4.13 \text{ g cm}^{-3}$  density. In particular, the  $c$ -axis of the  $\text{Al}_5\text{Mo}(r)$  phase is three times that of the  $\text{Al}_5\text{Mo}(h)$  phase [8]. These results obtained for the Al-10 at.% Mo alloy are consistent with the phase diagram of the Al-Mo system established by Schuster et al. [24].

As the Mo content increases to 30 wt.%, a significant decrease in the intensity of the characteristic Al peaks corresponding to the (111)Al and (200)Al planes, as well as an almost complete disappearance of the (220)Al and (311)Al peaks, can hardly be ignored, as shown in Fig. 2. Meanwhile, a more complex new phase,  $\text{Al}_{17}\text{Mo}_4$ , appears in the XRD patterns. According to the investigation by Schuster et al. [24], this phase is present in the cast and has a melting point of  $1130^\circ\text{C}$ . However, more recent experimental studies by Eumann et al. [14] indicate that the  $\text{Al}_{17}\text{Mo}$  phase is only stable at temperatures below  $1034^\circ\text{C}$ . This phase exhibits a monoclinic structure pertaining to the  $C2$  space group and is characterized by crystal parameters:  $a = 0.915 \text{ nm}$ ,  $b = 0.493 \text{ nm}$ ,  $c = 2.893 \text{ nm}$ , as well as a density of  $4.31 \text{ g cm}^{-3}$  [22].

### 3.2. Microstructure and EDS analysis

Metallographic observations made by optical microscopy (OM) and scanning electron microscopy (SEM) on pure Al and Al- $x$ Mo ( $x = 10, 30 \text{ wt.}\%$  Mo) alloys, as well as EDS analysis spectra of the phases formed, are presented in Figs. 3 and 4. It is undeniable that pure Al possesses a typical single-phase microstructure consisting of  $\alpha$ -Al solid solution. However, Al-Mo alloys with different Mo concentrations exhibit a dual-phase structure composed of an  $\alpha$ -Al matrix and an Al-Mo intermetallic phase. Furthermore, the morphology of the intermetallic phase in Mo-containing Al alloys varies with Mo concentration. In the Al-10Mo alloy, intermetallic particles appear mainly as needles of various sizes, uniformly dispersed in the matrix. According to the report by Qiu et al. [7], the needle-shaped particles are composed of two distinct phases: a brighter phase, identified as  $\text{Al}_5\text{Mo}(r)$ , surrounded by a lighter phase correspond-

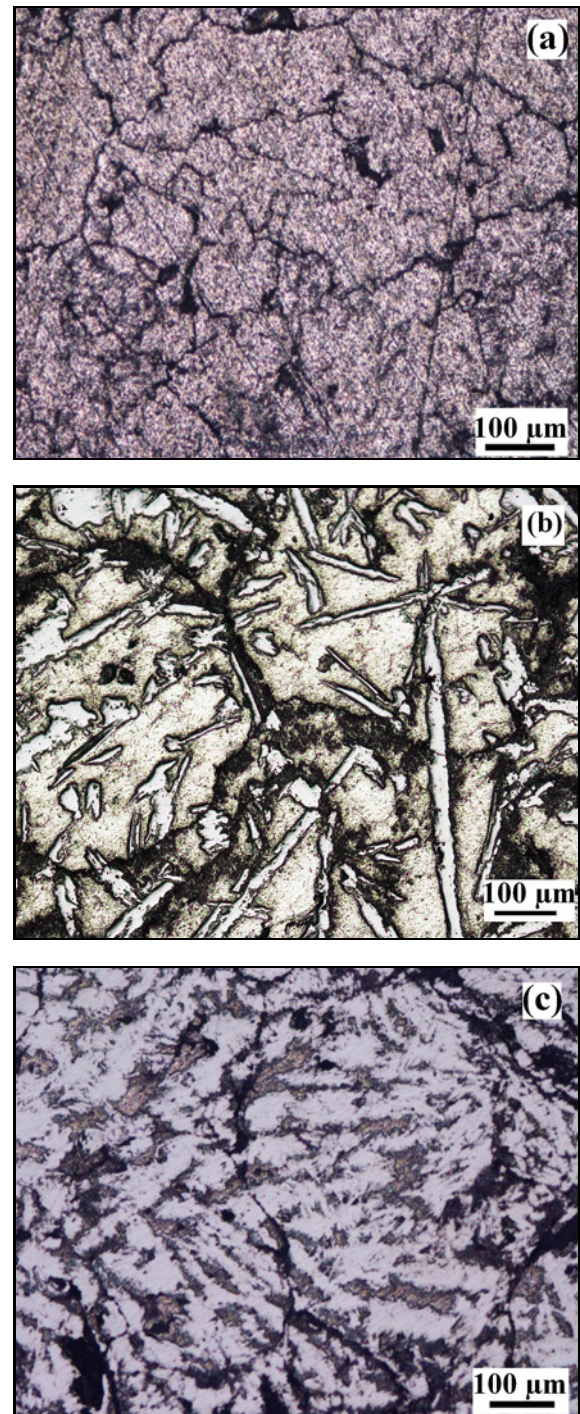


Fig. 3. OM micrographs of (a) Al, (b) Al-10 wt.% Mo, and (c) Al-30 wt.% Mo alloys.

ing to  $\text{Al}_{12}\text{Mo}$ . Apparently, with the consideration of the element concentration, the intermetallic particles mentioned are corresponding to the  $\text{Al}_5\text{Mo}(r)$  (bright phase) and the  $\text{Al}_{12}\text{Mo}$  (light phase). The faceted particles, present in marginal quantities, are composed of 87.41 at.% Al and 12.59 at.% Mo, naturally approaching the  $\text{Al}_7\text{Mo}$  phase. Overall, for the currently studied

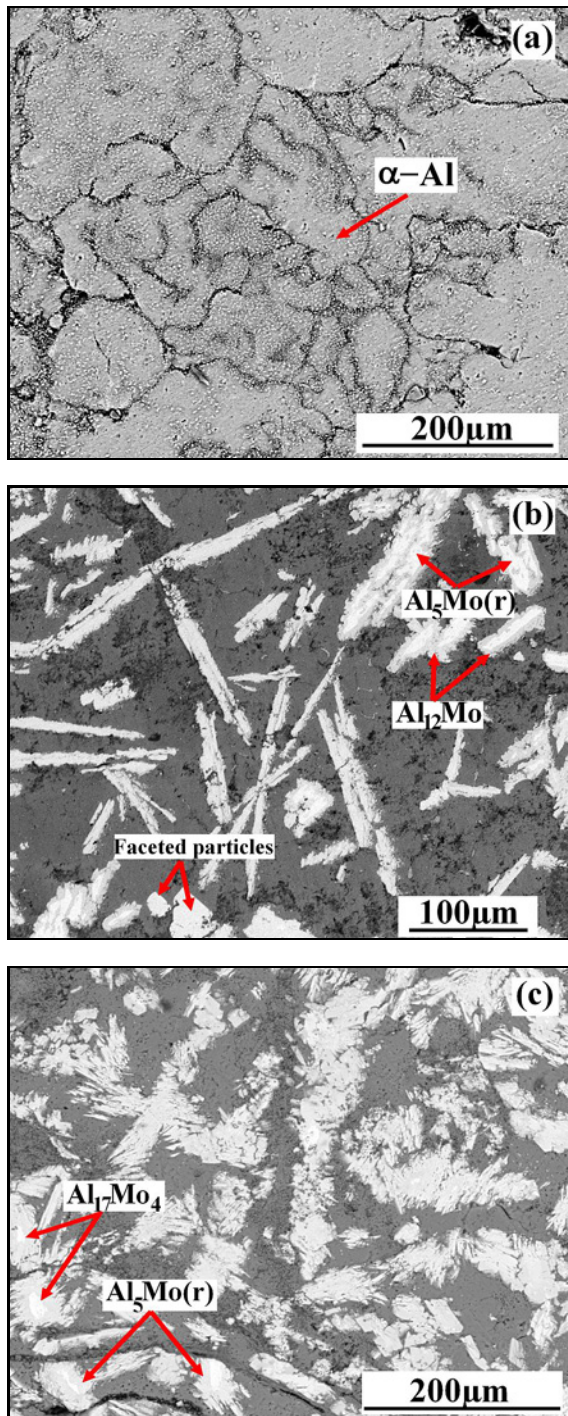


Fig. 4. SEM micrographs of (a) Al, (b) Al-10 wt.% Mo, and (c) Al-30 wt.% Mo alloys.

composition with 10 wt.% Mo addition, the preparation methods, either high-frequency magnetic melting or laser processing [6], only exert a very limited influence on the alloy's phase formation.

As the Mo content increases to 30 wt.% in the Al-Mo alloy, the amount of the intermetallic phase in the matrix dramatically increases, which appears only in

Table 1. EDS results for different phases

Sample	Phase	Composition of phases by EDS (at.%)	
		Al	Mo
Al	$\alpha$ -Al Matrix	100	–
Al-10Mo	$\alpha$ -Al Matrix	99.71	0.29
	$\text{Al}_{12}\text{Mo}$	92.25	7.75
	$\text{Al}_5\text{Mo}(r)$	83.19	16.81
Al-30Mo	$\alpha$ -Al Matrix	99.65	0.35
	$\text{Al}_5\text{Mo}(r)$	83.71	16.29
	$\text{Al}_{17}\text{Mo}_4$	81.95	18.05

dendritic form. Qiu et al. [7] reported that dendrites in the intermetallic phase divide into two forms, distinct in their geometry and growth dynamics. The so-named  $90^\circ$  dendrites have primary arms at approximately  $90^\circ$  to each other, with lateral branches at  $45^\circ$ . Their growth is asymmetrical, with the arms developing at different rates. These dendrites have a complex tetragonal structure, but their  $90^\circ$  configuration is unstable and evolves towards more stable structures. In contrast,  $30^\circ$  dendrites display a single direction of growth, with lateral branches forming angles of  $30^\circ$  or  $60^\circ$  to the primary arms. They are less ramified, have more elongated arms and a simpler morphology, and are considered stable forms resulting from the evolution of  $90^\circ$  dendrites. In this structure, the dendritic intermetallic phase is composed of two phases. The bright phase corresponds to  $\text{Al}_{17}\text{Mo}_4$ , surrounded by a clear phase identified as  $\text{Al}_5\text{Mo}(r)$ . Furthermore, it was found that the faceted particles disappeared, which is apparently different from those in the Al-10Mo alloy.

The EDS spectrum and quantitative data for the chemical constituents in the phases of pure Al and Al- $x$ Mo ( $x = 10$  and 30 wt.% Mo) alloy samples are presented in Fig. 5 and Table 1, respectively. In the Al-10Mo alloy, the  $\alpha$ -Al matrix is composed of 99.71 at.% Al and 0.29 at.% Mo. The  $\text{Al}_{12}\text{Mo}$  phase consists of 92.25 at.% Al and 7.75 at.% Mo, while the  $\text{Al}_5\text{Mo}$  phase contains 83.19 at.% Al and 16.81 at.% Mo [21]. Faceted particles have a composition of 87.41 at.% Al and 12.59 at.% Mo, approaching the  $\text{Al}_7\text{Mo}$  stoichiometry. According to Qiu et al. [7], this phase has an Fm $\bar{3}$ m crystal structure with a lattice parameter of approximately 1.45 nm, which does not correspond to any phases identified in the Al-Mo system.

For the Al-30Mo alloy, we observe an increase in Mo solubility in the Al matrix, attaining 0.35 at.% Mo. In addition to the  $\text{Al}_5\text{Mo}(r)$  phase, the  $\text{Al}_{17}\text{Mo}_4$  phase is present in this alloy, with a composition of 81.95 at.% Al and 18.05 at.% Mo [22, 24].

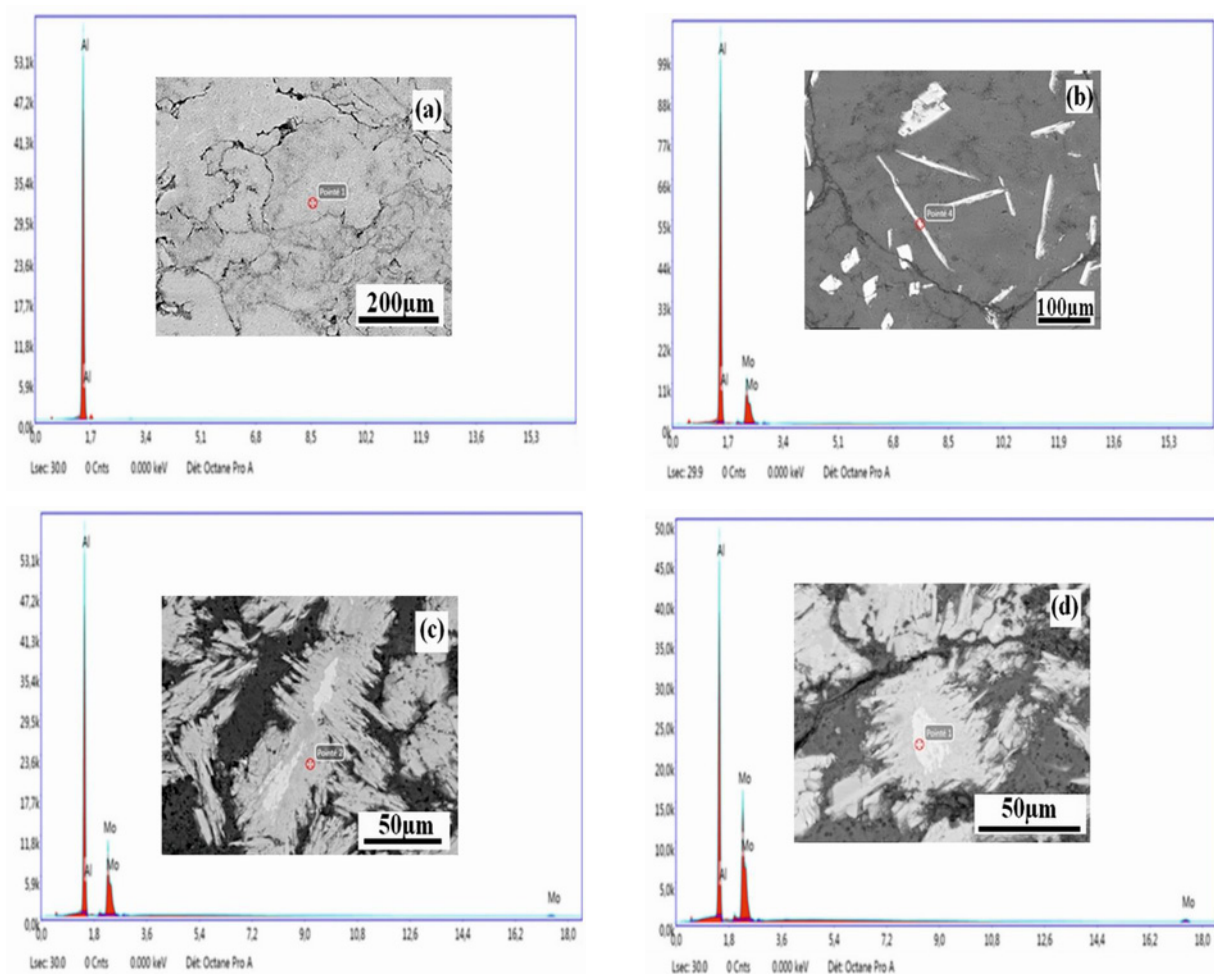


Fig. 5. EDS spectrum of different phases: (a)  $\alpha$ -Al matrix, (b)  $\text{Al}_{12}\text{Mo}$ , (c)  $\text{Al}_5\text{Mo}(r)$ , and (d)  $\text{Al}_{17}\text{Mo}_4$ .

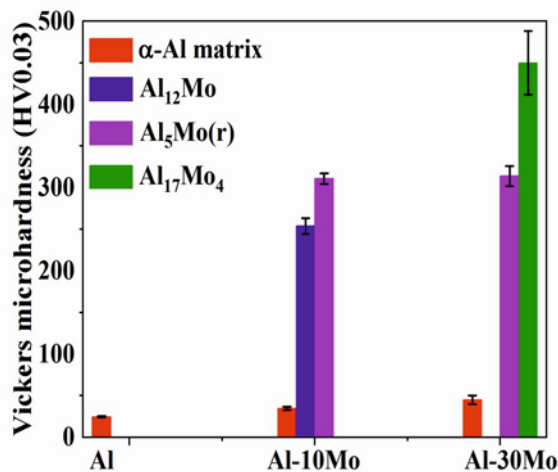


Fig. 6. Microhardness variation of phases.

### 3.3. Evolution of phase microhardness

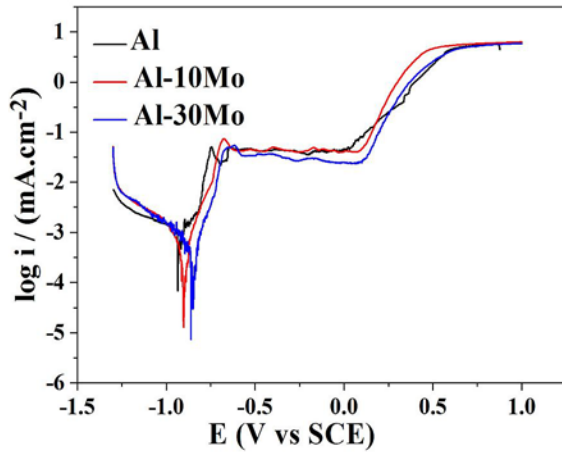
The microhardness of the different phases of the pure Al, Al-10Mo, and Al-30Mo structures (Fig. 6),

developed by high-frequency magnetic induction, reveals significant variations as a function of composition. The hardness of the  $\alpha$ -Al matrix in pure Al is 25 HV, but it increases with the addition of Mo to attain a maximum value around 45 HV for the Al-30Mo alloy. This improvement is attributed to the increased solubility of Mo in the Al matrix, which attains 0.35 at.% Mo in the Al-30Mo alloy. Mo exercises a direct hardening effect, whether in solid solution or in precipitated form, although this effect remains restricted by its low solubility in Al, which reaches around 0.07 at.% Mo.

However, rapid solidification techniques increase this solubility to 2.45 at.% Mo, thus improving mechanical properties [18]. Moreover, Mo plays an indirect role in stabilizing the grain structure, thereby contributing to a significant improvement in mechanical strength. Concerning  $\text{Al}_x\text{Mo}_y$  intermetallic phases present in Al-10Mo and Al-30Mo alloys, differences in hardness were observed. The  $\text{Al}_{17}\text{Mo}_4$  phase exhibits a higher hardness of 450 HV than  $\text{Al}_5\text{Mo}$  (314 HV) and  $\text{Al}_{12}\text{Mo}$  (254 HV). These variations can be explained by differences in crystallographic structure, chemical

Table 2. Corrosion parameters deduced from potentiodynamic polarization curves of Al- $x$ Mo ( $x = 0, 10, 30$  wt.% Mo) alloys in 3.5 % NaCl solution

Alloys	$E_{\text{corr}}$ (mV)	$I_{\text{corr}}$ ( $\mu\text{A cm}^{-2}$ )	$\beta_c$ (mV dec $^{-1}$ )	$\beta_a$ (mV dec $^{-1}$ )	Corrosion rate (mm year $^{-1}$ )
Al	$-935 \pm 8.86$	$0.856 \pm 0.05$	143.28	236.58	$0.0097 \pm 0.0032$
Al-10Mo	$-901 \pm 2.01$	$0.578 \pm 0.11$	125.8	181.75	$0.0063 \pm 0.0015$
Al-30Mo	$-861 \pm 5.53$	$0.294 \pm 0.06$	79.75	147.22	$0.0032 \pm 0.001$

Fig. 7. Potentiodynamic polarization curves for Al- $x$ Mo ( $x = 0, 10, 30$  wt.% Mo) alloys.

bond nature, and the thermodynamic conditions of phase formation.

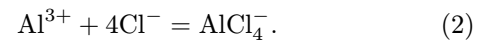
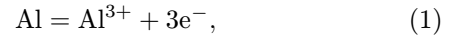
### 3.4. Electrochemical measurements

#### 3.4.1. Potentiodynamic polarization

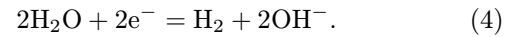
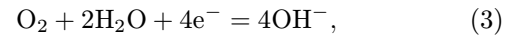
Adding transition metals to Al is an effective way to improve its resistance to pitting corrosion in chloride environments [25]. Several transition metals were investigated for this purpose, and Mo has distinguished itself as one of the most effective [26].

Figure 7 shows potentiodynamic polarization curves illustrating the effect of Mo addition on the electrochemical behavior of Al in a 3.5 % NaCl solution. The electrochemical measurements were performed after 1 hour of immersion at a scan rate of  $1 \text{ mV s}^{-1}$ . Corrosion potential ( $E_{\text{corr}}$ ) and corrosion current density ( $i_{\text{corr}}$ ) were determined using the Tafel extrapolation method.

Generally, the anodic dissolution of Al in a NaCl solution is a complex process, initiated by  $\text{Cl}^-$  ions attacking the alloy surface. This interaction leads to the formation of  $\text{Al}^{3+}$  ions, which combine with  $\text{Cl}^-$  ions to produce complexes such as  $\text{AlCl}_3$  and  $\text{AlCl}_4^-$ . This dissolution process occurs in several stages [27, 28]:



The cathodic reaction in 3.5 % NaCl solution is limited by oxygen transfer [28, 29]:



In the presence of Mo, we note that the corrosion potential shifts towards positive values. It passes from  $-935 \text{ mV/SCE}$  for pure Al to  $-901 \text{ mV/SCE}$  in the presence of 10 wt.% Mo, and continues to move towards nobler values with increasing Mo percentage, reaching  $-861 \text{ mV/SCE}$  in the presence of 30 wt.% Mo. All potentiodynamic polarization curves exhibit a passivation plateau in the anodic region.

This plateau results from the formation of a passive layer consisting of Al oxide ( $\text{Al}_2\text{O}_3$ ) on the alloy surface [30]. The intermetallic compounds formed in Al-Mo alloys, such as  $\text{Al}_{12}\text{Mo}$ ,  $\text{Al}_5\text{Mo}(r)$ , and  $\text{Al}_{17}\text{Mo}_4$ , influence the overall electrochemical behavior by creating chemical microheterogeneities on the alloy surface. These phases have an electrochemical potential different from that of the aluminum matrix, thereby generating local microgalvanic piles. However, their effect does not induce a significant increase in the passive domain, as indicated by the absence of an enlargement of the passivation plateau observed experimentally, confirming the results of Ghelloudj et al. [31].

From the electrochemical parameters obtained from polarization curves (Table 2), we note that the addition of Mo significantly reduces corrosion density, from  $0.85 \mu\text{A cm}^{-2}$  for pure Al to  $0.29 \mu\text{A cm}^{-2}$  for Al-30Mo alloy. Similarly, the corrosion rate decreases from  $0.009 \text{ mm year}^{-1}$  for pure Al to  $0.003 \text{ mm year}^{-1}$  for Al-30Mo alloy.

#### 3.4.2. Electrochemical impedance spectroscopy

Nyquist and Bode impedance diagrams of Al- $x$ Mo alloys ( $x = 0, 10, 30$  wt.% Mo) are shown in Figs. 8a–c, illustrating the formation of two capacitive loops. The first loop, observed at high frequency, is associ-

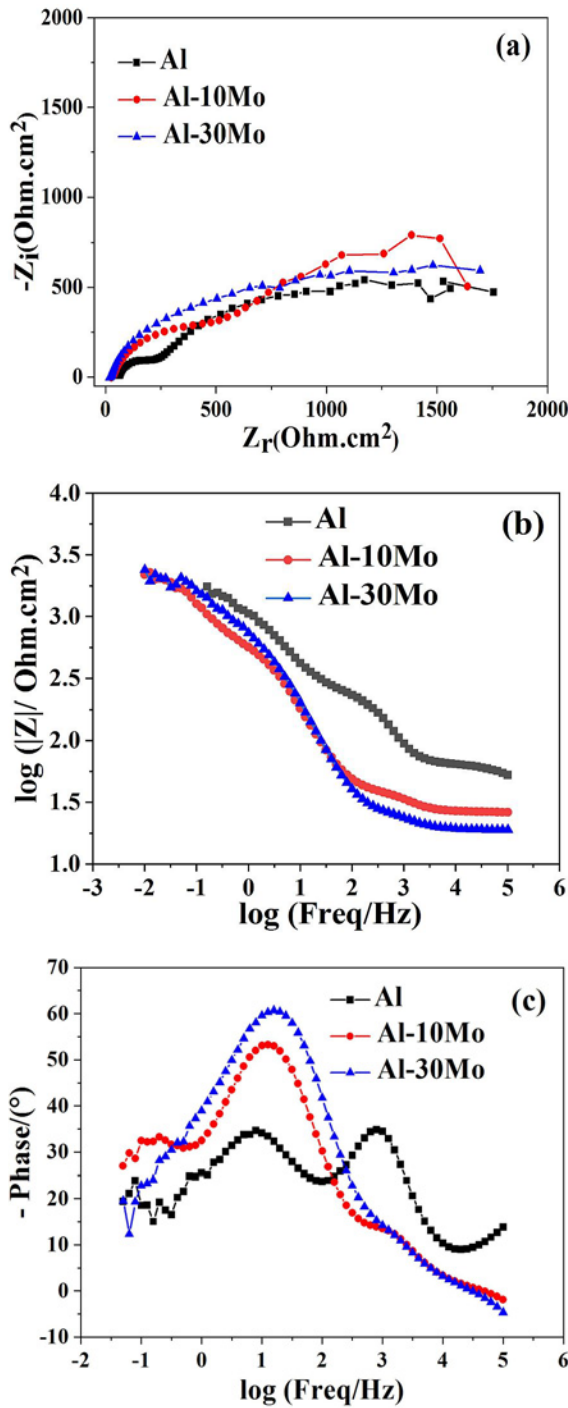


Fig. 8. Impedance diagrams of Al-*x*Mo (*x* = 0, 10, 30 wt.% Mo) alloys: (a) Nyquist curve, (b) Bode modulus plot, and (c) frequency phase-angle plot.

ated with the charge transfer mechanism. It is characterized by the charge-transfer resistance ( $R_{ct}$ ) and the capacitance of the electric double layer ( $Q_{dl}$ ) at the alloy-solution interface, both of which are related to sample degradation [32]. The second loop, observed at low frequency, results from the formation of a cor-

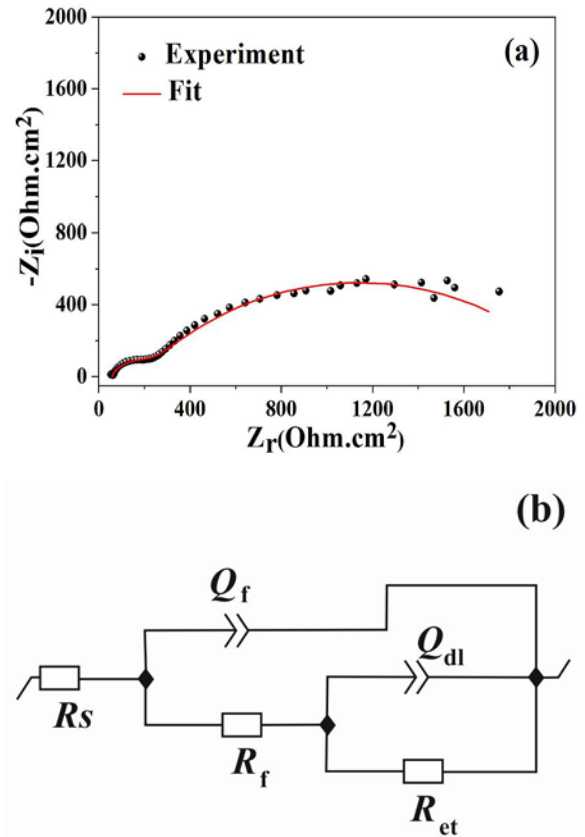


Fig. 9. (a) Fitted and experimental Nyquist plots of aluminum in 3.5 % NaCl and (b) electrochemical equivalent circuit used to fit the EIS spectra.

rosion product film on the alloy surface in solution [33]. It is defined by the film’s resistance ( $R_f$ ) and capacitance ( $Q_f$ ). Furthermore, Bode diagram analysis reveals that Al-*x*Mo alloys (*x* = 0, 10, and 30 wt.% Mo) exhibit two-phase angular peaks characteristic of reactive capacitance, suggesting the existence of dual time constants.

Parametric fitting of the impedance spectra (Fig. 9a) was carried out using the equivalent circuit illustrated in Fig. 9b. The fitted parameters are shown in Table 3. This circuit includes a solution resistance ( $R_s$ ), a resistance ( $R_f$ ), and a capacitance ( $Q_f$ ) corresponding to the layer of corrosion products on the sample surface, as well as a charge transfer resistance ( $R_{ct}$ ) and a double-layer capacitance ( $Q_{dl}$ ). The polarization resistance ( $R_p$ ) was calculated according to the following Eq. (5):

$$R_p = R_f + R_{ct}. \tag{5}$$

The results show that adding Mo increases the polarization resistance of Al. The order of  $R_p$  values was as follows: Al-30 wt.% Mo > Al-10 wt.% Mo > Al, indicating that the higher the Mo content, the better the



Table 3. Electrochemical parameters derived from equivalent circuit fitting of EIS curves

Alloys	$R_s$ ( $\Omega \text{ cm}^2$ )	$R_f$ ( $\Omega \text{ cm}^2$ )	$Q_f$ ( $\mu\text{F cm}^{-2}$ )	$n$	$R_{ct}$ ( $\Omega \text{ cm}^2$ )	$Q_{dl}$ ( $\mu\text{F cm}^{-2}$ )	$n$	$R_p$ ( $\Omega \text{ cm}^2$ )
Al	$58.1 \pm 0.26$	$201 \pm 2.55$	7.001	0.84	$1757 \pm 4.42$	174	0.65	$1958 \pm 5.65$
Al-10Mo	$27.6 \pm 1.83$	$904 \pm 4.07$	260	0.74	$1370 \pm 2.82$	1533	0.94	$2274 \pm 3.55$
Al-30Mo	$19.8 \pm 0.49$	$1010 \pm 5.27$	177	0.80	$1802 \pm 7.71$	1048	0.95	$2812 \pm 7.78$

corrosion resistance of the alloy, which is consistent with potentiodynamic polarization results.

#### 4. Conclusions

This work focuses on the elaboration and characterization of Al- $x$ Mo alloys ( $x = 0, 10, 30 \text{ wt.}\%$ ) melted by high-frequency induction. The main results obtained are as follows:

- The high-frequency magnetic induction melting technique increases the solubility of Mo in Al up to 0.35 at.% Mo, resulting in an increase in the hardness of the  $\alpha$ -Al matrix to 45 HV0.03.

- The structure of Al-Mo alloys maintains a solid  $\alpha$ -Al solution while favoring the formation of specific intermetallic phases such as  $\text{Al}_{12}\text{Mo}$ ,  $\text{Al}_5\text{Mo}(r)$ , and  $\text{Al}_{17}\text{Mo}_4$ .

- In the Al-10 wt.% Mo alloy, the intermetallic phases appear as needles, while in the Al-30 wt.% Mo alloy, they are present in dendritic form, covering the entire surface.

- The hardness of intermetallic phases varies according to their composition. The  $\text{Al}_{17}\text{Mo}_4$  phase has the highest hardness, attaining 450 HV0.03.

- Potentiodynamic polarization data indicate that the addition of Mo to Al improves its corrosion resistance in 3.5 % NaCl solution. This manifests in a shift in corrosion potential towards more positive values, a decrease in corrosion current density to  $0.29 \mu\text{A cm}^{-2}$  for the Al-30 wt.% Mo alloy, and a reduction in corrosion rate to  $0.003 \text{ mm year}^{-1}$ .

- Impedance results show that Mo addition increases the polarization resistance of Al- $x$ Mo alloys, indicating better corrosion protection. This improvement is related to the formation of a more protective corrosion product film and reduced charge transfer at the alloy-solution interface.

#### Acknowledgement

We want to thank the engineers at the National School of Technology and Engineering for their valuable assistance in characterizing the alloys.

#### References

- [1] M. Čavojský, P. Švec Sr., D. Janičkovič, L. Orovčík, F. Šimančík, Rapidly solidified Al-Mo and Al-Mn ribbons: Microstructure and mechanical properties of extruded profiles, *Kovove Mater.* 52 (2014) 371–376. <http://dx.doi.org/10.4149/km-2014-6-371>
- [2] M. H. Farshidi, M. Rifai, H. Miyamoto, Grain refinement, texture evolutions, and strengthening of a recycled aluminium alloy subjected to tube channel pressing, *Kovove Mater.* 61 (2023) 13–21. <https://dx.doi.org/10.31577/km.2023.1.13>
- [3] F. Han, C. Li, Y. Wang, Z. Pai, Y. Meng, M. Cao, Y. Liu, P. He, X. Ma, L. Xue, C. Wang, Comparative study on corrosion property of 2219 aluminum alloy sheet and additively manufactured 2319 aluminum alloy, *J. Mater. Res. Technol.* 30 (2024) 3178–3185. <https://doi.org/10.1016/j.jmrt.2024.04.036>
- [4] S. Sen, A. Ghosh, A. Ghosh, G. Shankar, A. F. Abd El Rehim, M. Ghosh, Investigation of the role of non-octahedral slip planes in tensile deformation behaviour of naturally aged aluminium 6061 alloy, *Met. Mater. Int.* (2025). <https://doi.org/10.1007/s12540-024-01873-9>
- [5] L. M. Cheng, W. J. Poole, J. D. Embury, D. J. Lloyd, The influence of precipitation on the work-hardening behavior of the aluminum alloys AA6111 and AA7030, *Metall. Mater. Trans. A* 34 (2003) 2473–2481. <https://doi.org/10.1007/s11661-003-0007-2>
- [6] M. J. Kriegel, A. Walnsch, O. Fabrichnaya, D. Pavlyuchkov, V. Klemm, J. Freudenberger, D. Rafaja, A. Leineweber, High-temperature phase equilibria with the bcc-type  $\beta$  (AlMo) phase in the binary Al-Mo system, *Intermetallics* 83 (2017) 29–37. <https://doi.org/10.1016/j.intermet.2016.12.004>
- [7] Y. Y. Qiu, A. Almeida, R. Vilar, Structure characterization of a laser-processed Al-Mo alloy, *J. Mater. Sci.* 33 (1998) 2639–2651. <https://doi.org/10.1023/A:1004317605718>
- [8] R. S. Rana, R. Purohit, S. Das, Reviews on the influences of alloying elements on the microstructure and mechanical properties of aluminum alloys and aluminum alloy composites, *Int. J. Sci. Res. Publ.* 2 (2012) 1–7.
- [9] A. Almeida, F. Carvalho, P. A. Carvalho, R. Vilar, Laser-developed Al-Mo surface alloys: Microstructure, mechanical and wear behaviour, *Surf. Coat. Technol.* 200 (2006) 4782–4790. <https://doi.org/10.1016/j.surfcoat.2005.04.045>
- [10] C. P. Chang, M. H. Loretto, Bulk and dislocation core diffusion in Al-Mo solid solutions obtained through rapid-solidification processing, *Philos. Mag. A* 57 (1988) 593–603. <https://doi.org/10.1080/01418618808214409>

- [11] B. Liao, X. Ouyang, H. Li, F. Yin, Z. Li, B. Yin, J. Hu, W. Zhang, Experimental investigation and thermodynamic calculation of the Co-Al-Mo ternary system, *J. Alloys Compd.* 945 (2023) 169114. <https://doi.org/10.1016/j.jallcom.2023.169114>
- [12] H. Okamoto, Al-Mo (Aluminum-Molybdenum), *J. Phase Equilib. Diffus.* 31 (2010) 492–493. <https://doi.org/10.1007/s11669-010-9758-9>
- [13] K. Bouhamla, A. Gharbi, O. Ghelloudj, M. Y. Debili, S. Remili, Development and characterization of Al-15 % Mo binary alloys, *J. Phys.: Conf. Ser.* 1818 (2021) 012161. <https://doi.org/10.1088/1742-6596/1818/1/012161>
- [14] M. Eumann, G. Sauthoff, M. Palm, Re-evaluation of phase equilibria in the Al-Mo system, *Int. J. Mater. Res.* 97 (2006) 1502–1511. <https://doi.org/10.1515/ijmr-2006-0235>
- [15] Z. Du, C. Guo, C. Li, W. Zhang, Thermodynamic description of the Al-Mo and Al-Fe-Mo systems, *J. Phase Equilib. Diffus.* 30 (2009) 487–501. <https://doi.org/10.1007/s11669-009-9564-4>
- [16] M. V. Zdujic, K. F. Kobayashi, P. H. Shingu, Structural changes during mechanical alloying of elemental aluminium and molybdenum powders, *J. Mater. Sci.* 26 (1991) 5502–5508. <https://doi.org/10.1007/BF00553650>
- [17] I. S. Lee, P. W. Kao, C. P. Chang, N. J. Ho, Formation of Al-Mo intermetallic particle-strengthened aluminum alloys by friction stir processing, *Intermetallics* 35 (2013) 9–14. <https://doi.org/10.1016/j.intermet.2012.11.018>
- [18] O. A. Abu-Zeid, R. I. Bates, Friction and corrosion resistance of sputter-deposited supersaturated metastable Al-Mo alloys, *Surf. Eng.* 12 (1996) 167–168. <https://doi.org/10.1179/sur.1996.12.2.167>
- [19] E. A. Logan, J. N. Pratt, M. H. Loretto, Metastable phase formation in rapidly solidified Al-Mo alloys, *Mater. Sci. Technol.* 5 (1989) 123–130. <https://doi.org/10.1179/mst.1989.5.2.123>
- [20] C. P. Chang, M. H. Loretto, The annealing behaviour of rapid solidification processed Al-Mo alloys, *Mater. Sci. Eng.* 98 (1988) 185–189. [https://doi.org/10.1016/0025-5416\(88\)90152-8](https://doi.org/10.1016/0025-5416(88)90152-8)
- [21] A. Almeida, F. Carvalho, P. A. Carvalho, R. Vilar, Laser-developed Al-Mo surface alloys: Microstructure, mechanical and wear behaviour, *Surf. Coat. Technol.* 200 (2006) 4782–4790. <https://doi.org/10.1016/j.surfcoat.2005.04.045>
- [22] P. Villars, Al-Mo Binary Phase Diagram 0–100 at.% Mo, Pauling file. In *Inorganic Solid Phases*, Springer Materials (online database), Springer, Heidelberg (2023). [https://materials.springer.com/isp/phase-diagram/docs/c\\_0103038](https://materials.springer.com/isp/phase-diagram/docs/c_0103038).
- [23] H. Wu, C. Li, C. Guo, Z. Du, Experimental study on phase relations in the Al-Mo-Nb ternary system, *J. Alloys Compd.* 960 (2023) 170931. <https://doi.org/10.1016/j.jallcom.2023.170931>
- [24] J. C. Schuster, H. Ipsier, The Al-Al<sub>3</sub>Mo<sub>3</sub> section of the binary system aluminum-molybdenum, *Metall. Trans. A* 22 (1991) 1729–1736. <https://doi.org/10.1007/BF02646496>
- [25] H. Liu, Y. Pan, C. Tang, M. Liu, X. Chen, W. Yang, H. Tang, Y. Zhan, Experimental phase diagram of the Al-Mo-Gd ternary system at 773 K, *J. Phase Equilib. Diffus.* 36 (2015) 218–223. <https://doi.org/10.1007/s11669-015-0375-5>
- [26] T. Tsuda, C. L. Hussey, G. R. Stafford, Electrodeposition of Al-Mo alloys from the Lewis acidic aluminum chloride-1-ethyl-3-methylimidazolium chloride molten salt, *J. Electrochem. Soc.* 151 (2004) C379. <https://doi.org/10.1149/1.1704611>
- [27] M. Janik-Czachor, A. Wolowik, Z. Werner, Breakdown of passivity of Al-Mo glassy metals, *Mater. Sci. Forum* 185 (1995) 1049–1056. <https://doi.org/10.4028/www.scientific.net/MSF.185-188.1049>
- [28] Z. Zhang, P. Gan, D. Zhang, L. Gao, Experimental and theoretical investigations of the anti-corrosion film derived from bio-based melatonin on AA5052 aluminum alloy surface, *Colloids Surf. A* 691 (2024) 133880. <https://doi.org/10.1016/j.colsurfa.2024.133880>
- [29] D. Zhang, Z. Yan, L. Gao, Z. Xin, Y. Zhu, W. Wu, Corrosion behavior of AA5052 aluminum alloy in the presence of heavy metal ions in 3.5 % NaCl solution under negative pressure, *Desalination* 570 (2024) 117082. <https://doi.org/10.1016/j.desal.2023.117082>
- [30] C. C. Pan, D. H. Xia, M. Y. Hou, Z. Qin, Y. Xu, Y. Behnamian, W. Hu, Cavitation erosion of the AA7050 aluminum alloy in 3.5 wt.% NaCl solution—Part 1: mitigating effect by corrosion, *Corros. Sci.* 232 (2024) 112012. <https://doi.org/10.1016/j.corsci.2024.112012>
- [31] O. Ghelloudj, A. Gharbi, K. Bouhamla, M. Y. Debili, D. Zelmati, C. E. Ramouel, T. Chouchane, Study of the structure and corrosion behavior of Al-15%Mo alloy, *J. Phys.: Conf. Ser.* 1818 (2021) 012156. <https://doi.org/10.1088/1742-6596/1818/1/012156>
- [32] E. L. Principe, B. A. Shaw, G. D. Davis, Role of oxide/metal interface in corrosion resistance: Al-W and Al-Mo systems, *Corrosion* 59 (2003) 295–313. <https://doi.org/10.5006/1.3277562>
- [33] B. Zhou, C. Zhang, L. Yang, D. Bai, E. O. Olugbade, G. Z. Huang, Corrosion behaviour and mechanism of 6082 aluminium alloy in NaCl and Na<sub>2</sub>SO<sub>4</sub> etchants, *Mater. Corros.* 71 (2020) 392–400. <https://doi.org/10.1002/maco.201911185>
- [34] Y. Liu, R. Yue, L. Yang, Z. Song, Effects of various rolling deformations on the microstructure, mechanical properties, corrosion behavior, and cytocompatibility of biodegradable Zn-0.5Mn alloys, *Corros. Commun.* 18 (2025) 1–18. <https://doi.org/10.1016/j.corcom.2024.04.001>